MDPI

Article

Exploring γ-Ray Flares from High-Redshift Blazar B3 1343+451 at GeV Energies

Xiongfei Geng [1,2,3], Yang Liu [4], Gang Cao [5,*,†], Jing Fan [1,*,†,‡,§], Xiongbang Yang [5], Nan Ding [6], Minghu Gao [1,2], Yehui Yang [1,2] and Zhijie Zhang [7]

1   School of Electrical and Information Technology, Yunnan Minzu University, Kunming 650504, China; xiongfeigeng@ymu.edu.cn (X.G.); 040711@ymu.edu.cn (M.G.)
2   Yunnan Key Laboratory of Unmanned Autonomous System, Yunnan Minzu University, Kunming 650504, China
3   Yunnan Provincial Department of Education Engineering Research Center for Building Digital and Energy Saving Technology, Yunnan Minzu University, Kunming 650504, China
4   School of Physics and Astronomy, Yunnan University, Kunming 650091, China; liuyang@mail.ynu.edu.cn
5   Department of Mathematics, Yunnan University of Finance and Economics, Kunming 650221, China; xbyang@ynufe.edu.cn
6   School of Physical Science and Technology, Kunming University, Kunming 650214, China
7   Department of Astronomy and Jiujiang Research Institute, Xiamen University, Xiamen 361005, China; zhijiezhang@stu.xmu.edu.cn
*   Correspondence: gcao@ynufe.edu.cn (G.C.); 040658@ymu.edu.cn (J.F.)
†   These authors contributed equally to this work.
‡   Current address: University Key Laboratory of Information and Communication on Security Backup and Recovery, Yunnan Minzu University, Kunming 650500, China.
§   Current address: Wu Zhonghai Expert Workstation (No. 202305AF150045), Educational Instruments and Facilities Service Center, Educational Department of Yunnan Province, Kunming 650221, China.

Abstract: We study the temporal and spectral variability properties of the high-redshift blazar B3 1343+451 utilizing Fermi-LAT data from 2008 to 2022 in the energy range of 0.1–300 GeV. We identify six major flares with many substructures and analyze their temporal and spectral properties in detail. The fastest rise and decay timescales are found to be 4.8 ± 0.48 h and 5.28 ± 0.72 h, respectively. The size of the emission region is constrained to be $R \sim 5.18 \times 10^{15}$–$1.56 \times 10^{16}$ cm with the typical Doppler factors of $\delta \sim 10$–30. Most of the peaks from the flares exhibit a symmetric temporal profile within the error bars, implying that the rise and decay timescales are dominated by the disturbances caused by dense plasma blobs passing through the standing shock front in the jet region. We also find that four flares are better fitted with a log-parabolic distribution, while two flares are better fitted with a power-law distribution. Our results indicate that the emission regions vary from one flare to another, which is consistent with earlier results.

Keywords: blazars; γ-ray; active galactic nuclei; B3 1343+451

1. Introduction

Blazars, as a subclass of powerful radio-loud active galactic nuclei (AGNs) where the relativistic jet aligns very closely with the observer's line of sight, are considered as the potential sources of astrophysical high-energy cosmic rays and neutrinos [1,2]. Their broadband electromagnetic radiation is dominated by non-thermal emission from radio-to-high energy (HE), and even very-high-energy (VHE), γ-ray bands [3]. The non-thermal emission from these objects often exhibits distinctive observational characteristics, such as minute-scale variability and compact radio emission in the γ-ray band, etc. [4–7], which can reveal underlying physical information, such as the location and size of the emission region and the dynamics of the jet, etc. [8–10].

Blazars are usually divided into two major categories by their optical spectrum and spectral energy distribution (SED) [11,12], namely, Flat-Spectrum Radio Quasars (FSRQs)

with strong emission lines and BL Lacertae objects (BL lacs) with weak emission lines [13]. In the Fourth Catalog of Active Galactic Nuclei—Data Release 3 (4LAC-DR3), more than 5000 blazars are recorded [14] in the high-energy γ-ray band. Based on the position of the synchrotron peak in the rest frame (ν_{syn}^{peak}), blazars are further classified as high synchrotron peaked (HSP, for $\nu_{syn}^{peak} > 10^{15}$ Hz), intermediate synchrotron peaked (ISP, for $10^{14} < \nu_{syn}^{peak} < 10^{15}$ Hz), and low synchrotron peaked (LSP, for $\nu_{syn}^{peak} < 10^{14}$ Hz) [15].

Multi-wavelength observational results have shown that the SEDs of blazars exhibit a double-peaked structure; the low-energy peak is between the infrared and *X*-ray bands, while the high-energy peak is located at MeV-GeV energies. The origin of the low-energy peak is generally ascribed to the synchrotron emission of relativistic electrons in the jet, while the nature of the high-energy peak is still debated. Two kinds of models, the leptonic model and the hadronic model, have been developed to explain the blazar high-energy peak. In the leptonic model, the high-energy peak is produced by inverse Compton (IC) scattering of relativistic electrons that up-scatter the low-energy seed photons. If the seed photons are the synchrotron photons, this scenario is called a synchrotron self-Compton model (SSC). If the seed photons are derived from an external jet, such as the non-thermal emission from the disk, torus, broad-line region (BLR), and/or Cosmic Wave Background Radiation, this scenario is called an external Compton model [12,16–20]. In the hadronic model, the high-energy emission is produced by a proton synchrotron or secondary emission from proton–proton (pp) or proton–photon interactions [20–24].

Blazar B3 1343+451 (4FGL name J1345.5+4453c, RA:206.39, Dec: 44.88) is classified as an FSRQ. Its redshift is $z \sim 2.534$. The *Fermi*-LAT has detected four γ-ray flaring states for this source, namely from MJD 55,083 to 55,116, from 55,839 to 55,965, from 56,160 to 56,235, and from 57,021 to 57,126. In the first year after the *Fermi* satellite's launch, the flux of the source was at a low stage, with an average flux of $F_{>100MeV} \sim 1.5 \times 10^{-7}$ ph cm^{-2} s^{-1}. On 5 December 2011 and on 13 December 2009, strong flares from the source were detected with a peak flux of $F_{>100MeV} \sim 8.8 \times 10^{-7}$ ph cm^{-2} s^{-1}. The shortest flux halving time of $\sim$2.34 days and the hardest photon index of $\sim$1.73 $\pm$ 0.24 were found. The size of the γ-ray emission region can be constrained as $\sim$3.43 $\times 10^{16}$ cm. The results from Sahakyan et al. (2020), who performed the broadband SED modeling of B3 1343+451, show that the γ-ray emission regions are located outside the molecular torus (MT) [11]. They assumed that the observed flares are due to the change from the bulk Lorentz factor of the emitting region. These studies mainly focus on the long time variability, which obscures some physical information.

A detailed study of the outburst phases, short-timescale characteristics, spectral evolution, and flux distribution for this blazar has yet to be presented in the literature. Motivated by the strong outburst activity exhibited by B3 1343+451, we mainly focus on the individual outburst phases of B3 1343+451 observed from 2008 to 2021. We identify the outburst phases of B3 1343+451 by the Bayesian block (BB) algorithm with $E > 100$ MeV, and analyze the short-timescale characteristics from these outburst phases in detail. We also discuss the possible physical mechanism of these γ-ray flares. Section 2 presents a brief description of the observations and the data reduction procedure. Section 3 presents the characteristics of the γ-ray variability. Section 4 presents the characteristics of the γ-ray spectra. The main results are given and discussed in Section 5. Finally, a summary is given in Section 6.

2. *Fermi*-LAT Observations and Data Reduction

The Large Area Telescope (LAT) on board the *Fermi* satellite is a pair-conversion detector which is sensitive to photon energies from 20 MeV to more than 300 GeV. It surveys the whole sky every 3 h with an effective area of $\sim$8000 cm^2/GeV photon and a field of view of $\sim$2.4 sr [25]. In this work, we collect the first 14 years of data (from 2008 to 2022) for B3 1343+451 in the 0.1–300 GeV energy range by using the *Fermi*-LAT public data server[1].

Following the standard analysis procedure, the Pass 8 *Fermi*-LAT γ-ray data for B3 1343+451 are analyzed by using the P8R3_SOURCE_V3 instrument response func-

tion. Photons are selected in a circular region of interest (ROI) of 15° radius centered at the location of B3 1343+451. According to the *Fermi-LAT* team's recommendation, good data and time intervals are calculated using the recommended *gtselect* "Event class=128" and "evtype=3" and *gtmktime* "(DATA_QUAL>0)&&(LAT_CONFIG==1)" tools. To avoid the γ-ray detection from the earth's limb, a zenith angle cut of ≤90° is used. We also use "make4FGLxml.py" to obtain the input model file with the isotropic background *iso_P8R3_SOURCE_V3_v1.txt* and the galactic diffuse emission model *gll_iem_v07.fits*[2]. The model file of each source is generated using the 4FGL-DR3 version. The spectral parameters set for the sources located within the ROI are allowed to be free in the analysis.

Fluxes and spectra with different timescales (7 days, 2 days, 1 day) are obtained by using an unbinned likelihood method. For the 7-day binning, the normalizations of the galactic diffuse and isotropic emission are taken as a free parameter, while, for the short-timescale variability with the 1-day and 2-day time bins, we fix the normalizations of the galactic diffuse and isotropic emission. We use the values of the test statistic, (TS) [26] defined as TS = $2 \times (log L_1 - log L_0)$, to obtain the source detection significance. We also perform spectral analyses using data from several epochs by fitting the γ-ray spectra in the energy range 0.1–300 GeV with power law (PL), log-parabola (LP), and PL with an exponential cutoff (PLEC) models. Definitions of these models are given on the FSSC website[3]. The energy of the highest-energy photon is calculated by using the "*gtsrcprob*" tool and the model file obtained from the likelihood fitting.

3. γ-Ray Variability of B3 1343+451

In this work, we identify the flares by using the Bayesian block algorithm with a false alarm rate parameter of $p_0 = 0.01$ (>3σ) [7,8,27,28]. Based on this algorithm, we find that the weekly binned γ-ray light curves exhibit six significant flares with fluxes in excess of 5×10^{-7} ph cm^{-2}s^{-1}, as shown in Figure 1a, Flare-I (MJD 55,040.66–55,180.66, 28 July 2009–15 December 2009), Flare-II (MJD 55,837.66–55,933.66, 3 October 2010–7 January 2012), Flare-III (MJD 56,131.66–56,195.66, 23 July 2012–25 September 2012), Flare-IV (MJD 56,621.66–56,733.66, 25 November 2013–17 March 2014), Flare-V (MJD 57,013.66–57,132.66, 22 December 2014–20 April 2015), Flare-VI (MJD 58,395.66–58,752.66, 4 October 2018–26 September 2019), which are similar to the results of Wu et al. [29] with a false alarm rate parameter of $p_0 = 0.05$ (>3σ), implying that the six flares are available.

We adopt `gtsrcprob` to obtain high-energy photons ($E \geqslant 10$ GeV) with >95% probabilities of being associated with the source. Figure 1d shows that the high-energy photons are observed during the flare period. The highest photon energy of 50.30 GeV is found with a significance level of 99.67% at MJD 55,884.22 during Flare-II. The strongest flaring state occurs in the Flare-III stage, with the highest photon energy of 49.02 GeV having a significance level of 99.90% at MJD 56,163.29.

To further study the temporal characteristics of each flare, we extract the one- and two-day binned substructure light curves of these flare epochs. We find that significant flux errors are observed in the two-day binned light curve of Flare-IV. So, we fit the two-day binned light curves of Flare-I, Flare-III, Flare-V, and Flare-VI and the one-day binned light curves of Flare-II with the following function:

$$F(t) = 2\,F_0 \left[e^{(T_0-t)/T_r} + e^{(t-T_0)/T_f} \right]^{-1}$$
$$+ 2\,F_1 \left[e^{(T_1-t)/T_{r_1}} + e^{(t-T_1)/T_{f_1}} \right]^{-1} \tag{1}$$
$$+ \cdots,$$

where F_0 is the flux at time T_0, which represents the approximate flare amplitude. T_r and T_f represent the characteristic timescale of the rise and decay from the flares, respectively. The time at the maximum flux value is calculated with the parameters of Equation (1). To validate the fit of each period, we calculate the corresponding residuals between the data and the best-fitting model. We use the equation $\xi = \frac{T_f - T_r}{T_f + T_r}$ to describe the symmetry of a

flare, where $|\xi| < 1$. For markedly symmetric flares, $|\xi| < 0.3$; for moderately asymmetric flares, $0.3 < |\xi| < 0.7$; and, for markedly asymmetric flares, $0.7 < |\xi| < 1$. The fitting parameters are given in Table 1.
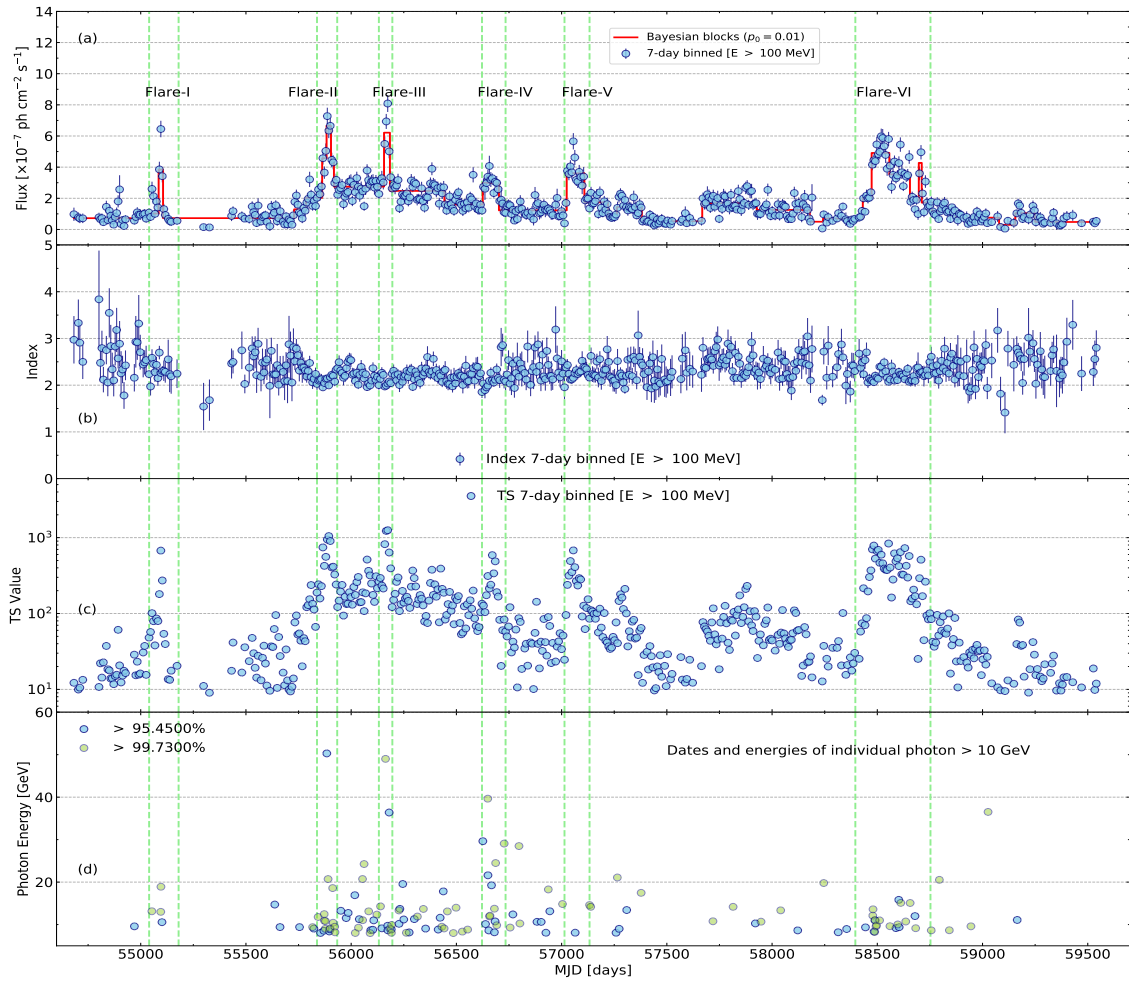

Figure 1. Panel (**a**) presents the 7-day binned light curves of B3 1343+451 from 2008 to 2022 at $E > 100$ MeV. The different patterns are divided by green vertical dashed lines. Panel (**b**) presents the γ-ray photon index as a function of time. Panel (**c**) presents the TS values (>9) as a function of time on a logarithmic scale. Panel (**d**) presents the arrival time and energy of $E > 10$ GeV photons with the significance levels of 2σ and 3σ.

We know that the statistical fluctuations tend to dominate the very short timescales. In order to fit the light curves of B3 1343+451 with multiple peaks, we first identify each individual peak from the 2-day binned light curves of Flare-I, Flare-II, Flare-V, and Flare-VI and 1-day binned light curves of Flare-III with a false alarm rate parameter of $p_0 = 0.05$ (95%) (see Figure A1 of Appendix A). We adopt Equation (1) to fit each peak individually and obtain the corresponding best-fitting parameters of the function. Afterward, multiple peaks in the light curves are fitted simultaneously with the best-fitting parameters from fitting each peak individually. In general, a lower χ^2/ndf (the number of degrees of freedom) value indicates a good fit between the model and the data. When the value of χ^2/ndf is too large, we add some substructure peaks to improve the fit. To validate the fit of each period, we also calculate the corresponding residuals between the data and the best-fitting model.

3.1. Flare-I

For a detailed study of Flare-I, we extract the 2-day binned light curve, as shown in the Figure 2a. In this period, we recognize three distinct peaks (P1, P2, and P3). Their

peak fluxes are (3.49 ± 0.71), (3.91 ± 0.99), and $(6.31 \pm 0.66) \times 10^{-7}$ ph cm^{-2} s^{-1} at MJD $55,057.42 \pm 0.71$, $55,089.05 \pm 0.71$, and $55,099.40 \pm 0.62$, respectively. The three peaks exhibit a marked symmetric temporal profile. All modeling parameters are described in Table 1.
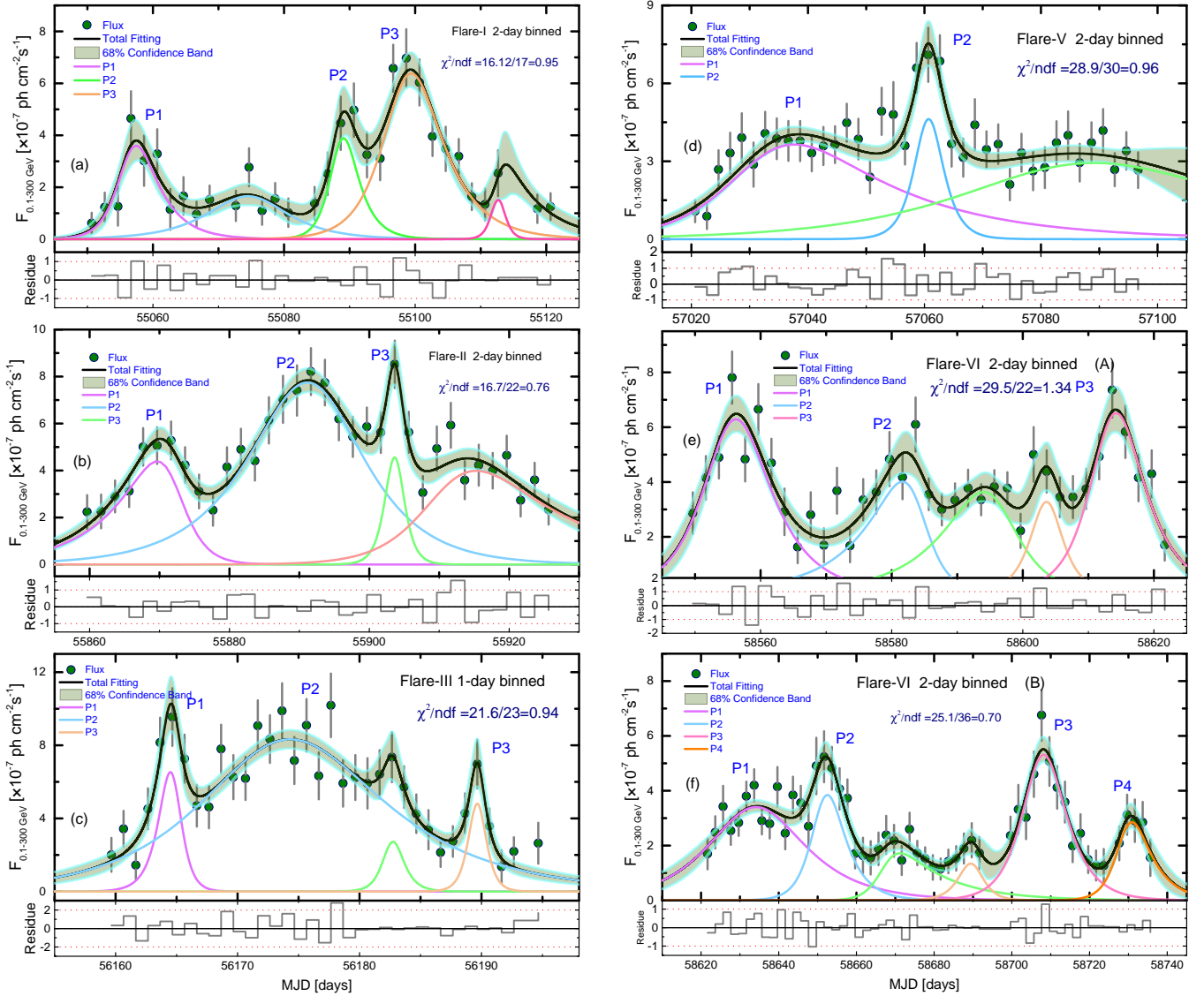

Figure 2. Panels (**a**,**b**,**d**–**f**) present the 2-day binned light curves of Flare-I, Flare-II, Flare-V, Flare-VI (A), and Flare-VI (B) that are identified in Figure 1, respectively. Panel (**c**) presents the 1-day binned light curves of Flare-III. The light curves are fitted with Equation (1). Here, the fitted residuals are shown in (**a**–**f**).

3.2. Flare-II

To understand the substructure during Flare-II, we obtain the 2-day binned light curve. Three subflares are exhibited during this period. The fit parameters are given in Table 1. The maximum peak flux is $(7.74 \pm 0.50) \times 10^{-7}$ ph cm^{-2} s^{-1} at MJD $55,891.14 \pm 0.96$.

Table 1. Best-fitting results of the 2-day and 1-day binned light curves of Flares-I–VI, as marked in Figures 1 and 2.

Peak	T_0 (MJD)	F_0 10^{-7} ph cm^{-2} s^{-1}	T_r (day)	T_f (day)	ξ	T_p (MJD)
			Flare-I			
P1	55,056.66	3.49 ± 0.71	2.00 ± 0.56	3.62 ± 1.55	0.29 ± 0.23	$55,057.42 \pm 0.71$
P2	55,088.66	3.91 ± 0.99	1.54 ± 0.63	2.35 ± 1.42	0.20 ± 0.35	$55,089.05 \pm 0.71$
P3	55,098.66	6.31 ± 0.66	3.32 ± 1.17	4.84 ± 0.65	0.19 ± 0.18	$55,099.40 \pm 0.62$
			Flare-II			
P1	55,871.66	3.80 ± 0.54	7.14 ± 1.18	2.22 ± 0.68	-0.52 ± 0.13	$55,869.68 \pm 0.36$
P2	55,891.66	7.74 ± 0.50	7.84 ± 0.99	6.81 ± 1.67	-0.07 ± 0.14	$55,891.14 \pm 0.96$
P3	55,903.66	4.85 ± 1.09	1.19 ± 0.42	1.14 ± 0.47	-0.02 ± 0.27	$55,903.63 \pm 0.32$
			Flare-III			
P1	56,164.66	6.72 ± 1.44	0.95 ± 0.29	0.65 ± 0.24	-0.19 ± 0.23	$56,164.51 \pm 0.18$
P2	56,173.66	8.29 ± 0.49	6.04 ± 0.84	7.37 ± 0.88	0.10 ± 0.10	$56,174.32 \pm 0.60$
P3	56,189.66	5.18 ± 1.31	0.60 ± 0.23	0.60 ± 0.21	0.00 ± 0.26	$56,189.65 \pm 0.16$
			Flare-V			
P1	57,032.66	3.28 ± 0.73	7.13 ± 1.74	18.88 ± 8.60	0.45 ± 0.21	$57,037.70 \pm 3.01$
P2	57,060.66	4.75 ± 0.92	2.12 ± 0.64	2.24 ± 0.73	0.03 ± 0.22	$57,060.71 \pm 0.49$
			Flare-VI (A)			
P1	58,555.66	6.27 ± 0.61	4.04 ± 0.82	5.20 ± 0.96	0.12 ± 0.14	$58,556.23 \pm 0.61$
P2	58,583.66	3.46 ± 1.50	7.10 ± 2.02	2.12 ± 1.55	-0.54 ± 0.28	$58,581.68 \pm 0.60$
P3	58,613.66	6.48 ± 0.77	3.14 ± 1.04	4.32 ± 0.71	0.15 ± 0.18	$58,614.23 \pm 0.60$
			Flare-VI (B)			
P1	58,633.66	3.41 ± 0.21	10.60 ± 2.26	11.56 ± 5.33	0.04 ± 0.25	$58,634.14 \pm 2.88$
P2	58,651.66	3.83 ± 0.95	3.04 ± 1.24	4.73 ± 1.29	0.21 ± 0.23	$58,652.47 \pm 0.81$
P3	58,707.66	5.35 ± 0.46	4.49 ± 0.73	5.51 ± 0.67	0.10 ± 0.10	$58,708.16 \pm 0.48$
P4	58,729.66	2.76 ± 0.43	2.75 ± 0.94	5.36 ± 1.72	0.32 ± 0.21	$58,730.87 \pm 0.80$

3.3. Flare-III

A 1-day binned light curve is generated to analyze Flare-III. In this period, three distinct peaks, P1, P2, and P3, are found at MJD $56,164.51 \pm 0.18$, $56,174.32 \pm 0.60$, and $56,189.65 \pm 0.16$, and have flux values of (6.72 ± 1.44), (8.29 ± 0.49), and $(5.18 \pm 1.31) \times 10^{-7}$ ph cm^{-2} s^{-1}, respectively. The three peaks exhibit a marked symmetric temporal profile.

3.4. Flare-V

We recognize two distinct peaks (P1 and P2) in the 2-day binned light curves. The flux values of these peaks are (3.28 ± 0.73) and $(4.75 \pm 0.92) \times 10^{-7}$ ph cm^{-2} s^{-1} at MJD $57,037.70 \pm 3.01$ and $57,060.71 \pm 0.49$, respectively. The decay timescale of peak P2 is longer than the rise timescale, implying an asymmetric temporal profile. On the contrary, peak P1 has a symmetric temporal profile. All modeling parameters are described in Table 1.

3.5. Flare-VI

Flare-VI is the longest-duration (MJD 58,395.66–58,752.66) activity phase of the $\sim$1 year light curve history. Flare-VI (A) has three prominent major peaks, which are labeled as P1, P2, and P3. The maximum peak flux is $(6.48 \pm 0.77) \times 10^{-7}$ ph cm^{-2} s^{-1} at MJD $58,614.23 \pm 0.60$. The rise timescale of peak P2 is longer than the decay timescale, implying an asymmetric temporal profile. Flare-VI (B) exhibits four distinct peaks (P1, P2, P3, and P4), and the maximum peak flux is $(5.35 \pm 0.46) \times 10^{-7}$ ph cm^{-2} s^{-1} at MJD $58,708.16 \pm 0.48$. All peaks show a marked symmetric temporal profile. All modeling parameters are described in Table 1.

3.6. Duration of the Shortest Flux Variability

To obtain the duration of the shortest flux variability, the 2-day and 1-day binned light curves are scanned by the comparison of consecutive light curve points using the following equation:

$$F(t_2) = F(t_1)2^{(\tau^{-1}(t_2-t_1))} \tag{2}$$

where doubling/halving (indicated by "+" and "-", respectively) the timescale is indicated by τ, and $F(t_2)$ and $F(t_1)$ are the fluxes at consecutive time instants t_2 and t_1, respectively. We use a condition to scan the one-day binned light curves; the flux is doubled/halved between two successive instants of time with the TS values of ≥ 25 (corresponds to $\sim 5\sigma$ detection). Scanning results are provided in Table 2. The fastest rise timescale is 0.20 ± 0.02 day (4.8 ± 0.48 h) during MJD 56,700.66–56,701.66, and the shortest decay timescale is -0.22 ± 0.03 day during MJD 58,561.66–58,562.66.

Table 2. The results of the minimum timescale of doubling/halving by scanning the 1-day binned light curves for each flare. Here, column (5) is the characteristic timescale, and it is estimated by Equation (2). Column (6) is the redshift-corrected doubling/halving timescale, namely, $\tau_z = \tau/(1+z)$. The uncertainty of the timescale is calculated by propagating the uncertainty in the flux and time values through Equation (2). Column 7 suggests whether the variability event is an increase (rise) or a decrease (decay) in the flux.

T_{start} (t_1) (MJD)	Flux Start (F_1) (10^{-7} ph cm^{-2} s^{-1})	T_{stop} (t_2) (MJD)	Flux Stop (F_2) (10^{-7} ph cm^{-2} s^{-1})	τ (day)	τ_z (day)	Rise/Decay
			Flare-I			
55,102.66	5.43 ± 1.24	55,103.66	2.72 ± 0.83	−1.00 ± 0.11	−0.40 ± 0.04	D
			Flare-II			
55,866.66	2.91 ± 0.95	55,867.66	7.12 ± 1.45	0.77 ± 0.11	0.31 ± 0.04	R
55,867.66	7.12 ± 1.45	55,868.66	3.34 ± 0.82	−0.91 ± 0.05	−0.36 ± 0.02	D
55,868.66	3.34 ± 0.82	55,869.66	6.80 ± 1.24	0.97 ± 0.09	0.38 ± 0.03	R
55,869.66	6.80 ± 1.24	55,870.66	3.19 ± 0.89	−0.91 ± 0.12	−0.36 ± 0.05	D
			Flare-III			
56,146.66	4.81 ± 1.48	56147.66	2.16 ± 1.00	−0.87 ± 0.17	−0.34 ± 0.07	D
			Flare-IV			
56,637.66	3.40 ± 1.33	56,638.66	1.28 ± 0.90	−0.71 ± 0.23	−0.28 ± 0.09	D
56,665.66	4.41 ± 1.30	56,666.66	1.71 ± 1.10	−0.73 ± 0.27	−0.29 ± 0.11	D
56,666.66	1.71 ± 1.10	56,667.66	3.51 ± 1.17	0.97 ± 0.42	0.38 ± 0.16	R
56,700.66	1.35 ± 0.67	56,701.66	5.32 ± 1.77	0.51 ± 0.06	0.20 ± 0.02	R
			Flare-V			
57,042.66	4.93 ± 1.18	57,043.66	2.24 ± 0.84	−0.88 ± 0.15	−0.35 ± 0.06	D
57,051.66	2.09 ± 0.37	57,052.66	4.68 ± 1.22	0.86 ± 0.09	0.34 ± 0.04	R
57,055.66	5.12 ± 1.34	57,056.66	1.73 ± 0.90	−0.64 ± 0.15	−0.25 ± 0.06	D
57,056.66	1.73 ± 0.90	57,057.66	5.37 ± 1.16	0.61 ± 0.16	0.24 ± 0.06	R
57,062.66	9.37 ± 1.61	57,063.66	4.50 ± 1.13	−0.94 ± 0.16	−0.37 ± 0.06	D
			Flare-VI			
58,480.66	7.14 ± 1.20	58,481.66	3.02 ± 0.81	−0.81 ± 0.09	−0.32 ± 0.04	D
58,545.66	2.74 ± 1.15	58,546.66	5.62 ± 1.30	0.97 ± 0.25	0.38 ± 0.10	R
58,547.66	5.38 ± 1.63	58,548.66	2.35 ± 0.97	−0.84 ± 0.11	−0.33 ± 0.04	D
58,554.66	4.47 ± 1.06	58,555.66	10.61 ± 1.48	0.80 ± 0.09	0.32 ± 0.04	R
58,555.66	10.61 ± 1.48	58,556.66	5.10 ± 1.10	−0.95 ± 0.10	−0.37 ± 0.04	D
58,561.66	7.54 ± 1.61	58,562.66	2.23 ± 0.83	−0.57 ± 0.07	−0.22 ± 0.03	D
58,587.66	3.97 ± 0.87	58,588.66	1.94 ± 0.70	−0.97 ± 0.19	−0.38 ± 0.08	D
58,588.66	1.94 ± 0.70	58,589.66	4.03 ± 0.91	0.95 ± 0.18	0.37 ± 0.07	R
58,601.66	3.40 ± 1.11	58,602.66	7.02 ± 1.65	0.96 ± 0.12	0.38 ± 0.05	R
58,617.66	5.72 ± 1.38	58,618.66	2.55 ± 1.01	−0.86 ± 0.16	−0.34 ± 0.06	D
58,642.66	2.25 ± 0.81	58,643.66	4.61 ± 1.03	0.97 ± 0.18	0.38 ± 0.07	R

3.7. Flux Variations at Different Energy Bands

It is interesting to note that the IC scattering occurs in the Thomson regime when the emission region is located in the molecular torus (MT) region, while it occurs in the Klein–Nishina (K-N) regime when the emission region is located within the broad-line region (BLR) [30,31]. This difference implies an energy-dependent cooling timescale for emission regions embedded in the MT region or BLR, and results in a time lag between the cooling of the MeV and GeV components for the γ-ray flare. To investigate the possibility of energy-dependent cooling timescales, we extract the γ-ray flux below and above 1 GeV energy from Flare-I to Flare-VI. The results are shown in Figure 3 with low-energy and high-energy fluxes. To obtain the potential time lag below and above the 1 GeV flux variations, we employ the Python command line tool developed by Sun et al. [32] to compute the

cross-correlation function (CCF)/discrete correlation functions (DCFs). This method does not need to interpolate in the temporal domain, and can be used to probe correlations in two time series data that are unevenly sampled. The unbinned discrete correlation functions (UDCFs) are defined with the following equation:
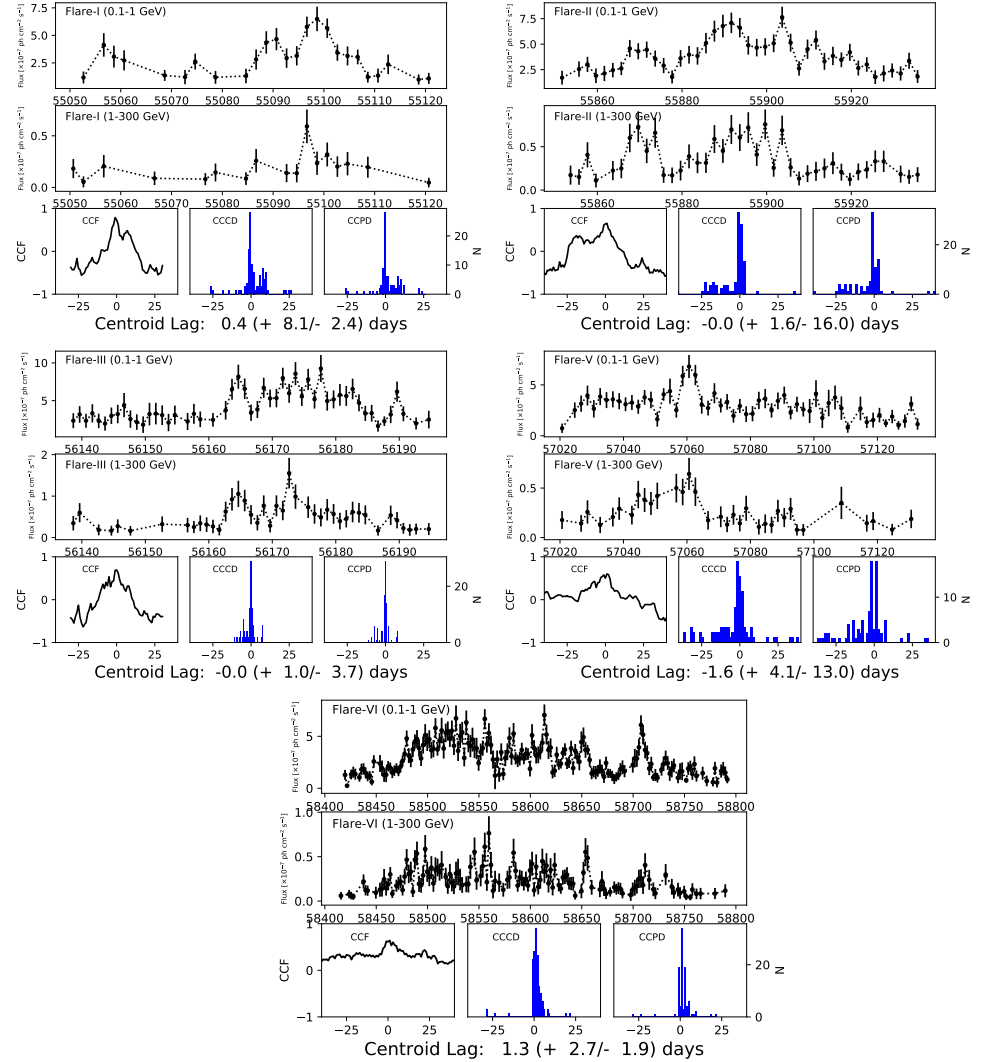

Figure 3. CCF calculated for the 2-day or 1-day light curves within the 0.1–1 GeV and 1–300 GeV energy bands. The top-left, top-middle, and top-right present the correlations of Flare-I (binned in 2-day periods), Flare-II (binned in 2-day periods), and Flare-III (binned in 1-day period), respectively. The bottom-left and bottom-right present the correlations of Flare-V (binned in 2-day periods) and Flare-VI (binned in 2-day periods). CCCD is the cross-correlation centroid distribution. CCPD is the cross-correlation peak distribution.

$$\mathrm{UDCF}_{ij} = \frac{(a_i - \bar{a})(b_j - \bar{b})}{\sqrt{(\sigma_a^2 - \mathrm{e}_a^2)(\sigma_b^2 - \mathrm{e}_b^2)}} \tag{3}$$

where a_i and b_i represent two discrete time series of the light curves, $\bar{a}$ and $\bar{b}$ are the means of the time series, and σ_a and σ_b are the standard deviations. e_a and e_b denote the measurement errors associated with each light curve. Each pair of $(a_i - b_i)$ is from the light curves that fall within the time lag bin defined by $\tau - \Delta\tau/2 \le \Delta t_{ij} \le \tau + \Delta\tau/2$, where

$\Delta t_{ij} = t_j - t_i$ is the pairwise lag, τ is the time lag, and $\Delta \tau$ is the bin width. The DCF of each time lag τ is defined as

$$\text{DCF}(\tau) = \frac{1}{M} \sum \text{UDCF}_{ij}(\tau) \tag{4}$$

where M is the number of pairs in the bin for which Δt_{ij}, the standard deviation of each bin, is defined as

$$\sigma_{\text{DCF}}(\tau) = \frac{1}{M-1} \sqrt{\sum \left[\text{UDCF}_{ij} - \text{DCF}_{ij}\right]^2} \tag{5}$$

The resultant DCFs for Flare-I to Flare-VI are shown in Figure 3. The uncertainty of the time lag is determined using a model-independent Monte Carlo method. We draw 10,000 random samples from a normal distribution for each data point of the light curve. Then, we generate 1000 subsets that are randomly sampled from the light curves, and obtain the time lags from $n = 1000$ simulations [33,34]. Based on 1000 time lags, we obtain a cross-correlation centroid distribution (CCCD) and a cross-correlation peak distribution (CCPD), as shown in Figure 3.

The light curves from Flare-I and Flare-VI between 0.1–1 GeV and 1–300 GeV exhibit positive time lags which are $0.4^{+8.1}_{-2.4}$ and $1.3^{+2.7}_{-1.9}$ days (top-left panel and bottom-right panel in Figure 3), implying that the 0.1–1 GeV flux is delayed with respect to the 1–300 GeV flux. However, the light curves from Flare-V exhibit negative time lags which are $-1.6^{+4.1}_{-13.0}$. It is worth pointing out that these delay times have a large amount of uncertainty in the DCF, implying that it is not possible to draw strong conclusions about the DCF peak at 0. To interpret any observed lag in the DCF as evidence for energy-dependent cooling timescales, we need to assume that the flux increasing in both energy bands occurs at the same time. A closer inspection of the light curves in Figure 3 (top-left panel and bottom-right panel) finds that the 0.1–1 GeV flux peaks $\sim$2 days before the 1–300 GeV flux. The DCFs for Flare-II and Flare-III seem to have a peak at a time lag of 0, which suggests that there is no energy dependence on the cooling timescale, implying that the γ-ray emission region is located in the BLR [35] with the IC scattering occurring in the Klein–Nishina regime.

4. SEDs of the Flares

The flares' SEDs are analyzed over several epochs of the flaring activity. We adopt two different photon spectra functions to fit the SEDs with the below form:

1. A power law (PL) defined as

$$dN(E)/dE = N_p \left(E/E_p\right)^{-\Gamma} \tag{6}$$

with E_p = 100 MeV.

2. A log-parabola (LP) defined as

$$dN(E)/dE = N_0 (E/E_0)^{-\alpha - \beta \ln(E/E_0)} \tag{7}$$

with E_0 = 300 MeV, where α is the photon index at E_0, and β is the curvature index.

Figure 4 exhibits the γ-ray spectra of the different states with the 7-day binned light curves. The γ-ray spectra show a clear deviation from the PL model except for Flare-I, which instead displays curvature features with the LP model. The significance levels of the spectral curvature from Flare-II, Flare-III, Flare-V, and Flare-VI are larger than 3σ. Similar results were also found for other *Fermi* blazars [7,8].

The origin of the γ-ray spectral curvature detected by the Fermi-LAT in many blazars is still an open question. Many theoretical models are proposed to explain the observed spectral curvature. Some are extrinsic factors, such as the attenuation of γ-rays via photon–photon pair production on He_{II} Lyman recombination lines in the BLR [36], the γ-γ absorption of $He_{II} + H_I$ from the full BLR [37], and a transition of inverse Compton scattering from the accretion disk (in the Thomson regime) to the disk emission reprocessed in the BLR (taking place in the Klein–Nishina regime). In this case, the γ-ray dissipation region lies inside the BLR. Sahakyan et al. (2020) modeled the spectral energy distribution

of B3 1343+451 with quiescent and flaring periods, and assumed a compact emitting region outside the BLR, implying that the above models do not explain the spectral curvature of B3 1343+451 [38–40]. However, using an equipartition approach, the observed spectral curvature may arise from the onset of Klein–Nishina effects on the Compton scattering of BLR photons, and, with the continuously curving electron energy distribution given by a log-parabola function, this continuously curving electron energy distribution derives from stochastic acceleration processes with radiation and escape [41]. In these intrinsic factors, the observed spectral curvature from B3 1343+451 is likely due to a cutoff in the energy distribution of particles that produce the γ-ray emission.
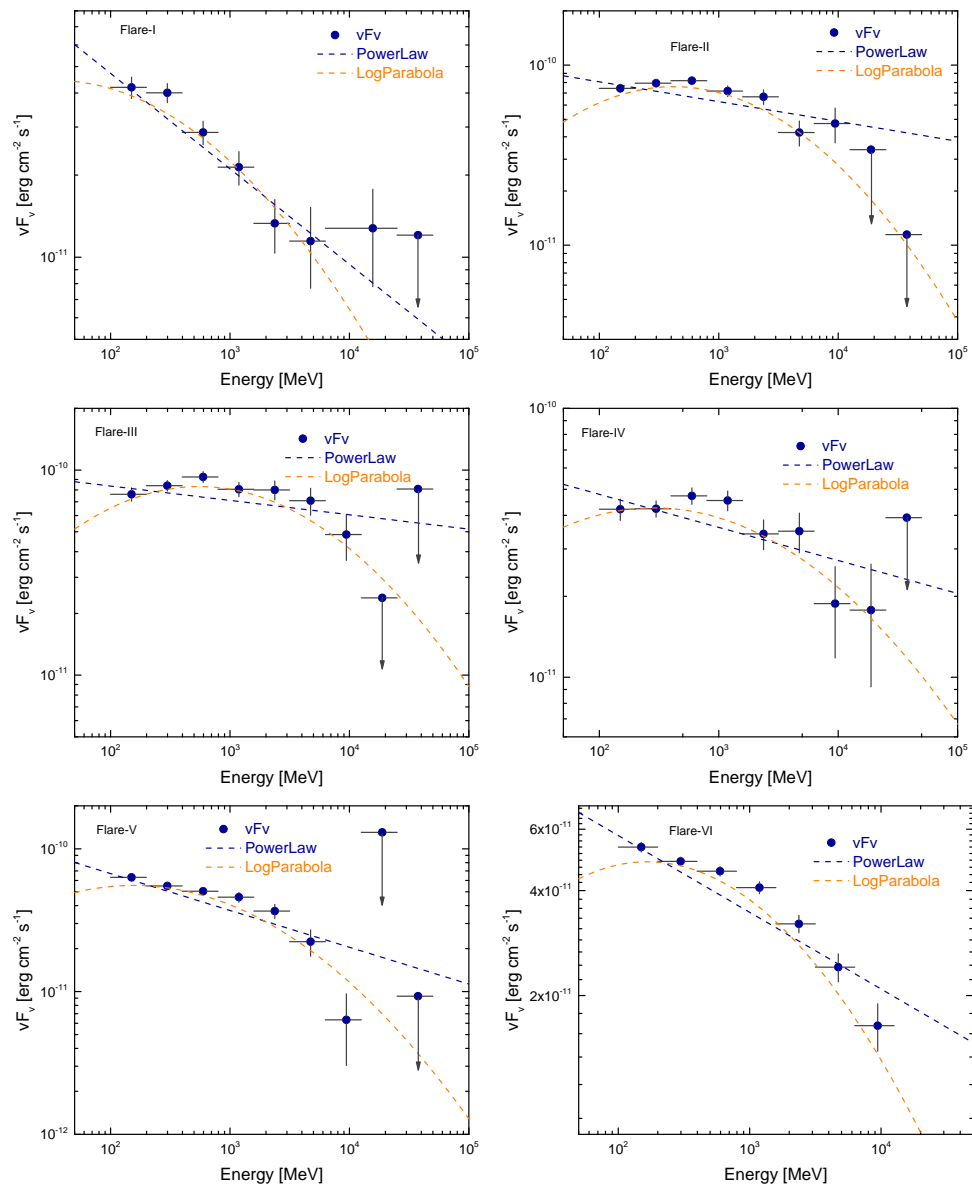
Figure 4. γ-ray SEDs of B3 1343+451 during the different states defined in Figure 1. These states are fitted by a PL (green lines) and LP (orange dashed curves). Their respective best-fitting parameters are given in Table 3.

Table 3. *Fermi*-LAT SEDs of the different activity states from the 7 d binned light curves, as defined in Figure 1.

Activity	F(> 100 MeV) (10⁻⁷ ph cm⁻² s⁻¹)	Γ	PL	TS	-Log(likelihood)	
Flare-I	2.18 ± 0.11	2.35 ± 0.04		1410.14	263,828.31	
Flare-II	4.54 ± 0.13	2.11 ± 0.02		6216.89	283,549.25	
Flare-III	4.89 ± 0.16	2.07 ± 0.03		4895.07	192,150.31	
Flare-IV	2.67 ± 0.11	2.12 ± 0.03		3133.49	319,569.29	
Flare-V	3.33 ± 0.11	2.26 ± 0.03		4085.73	342,531.76	
Flare-VI	2.94 ± 0.05	2.22 ± 0.01		15,868.70	1,572,236.40	
Activity	F(> 100 MeV) (10⁻⁶ ph cm⁻² s⁻¹)	α	LP β	TS	-Log(likelihood)	ΔLog(likelihood)
Flare-I	2.12 ± 0.11	2.26 ± 0.07	0.06 ± 0.03	1412.02	263,826.34	−1.97
Flare-II	4.29 ± 0.13	1.93 ± 0.04	0.10 ± 0.02	6237.64	283,531.64	−17.60
Flare-III	4.63 ± 0.17	1.90 ± 0.02	0.08 ± 0.02	4911.49	192,138.98	−11.33
Flare-IV	2.55 ± 0.11	2.01 ± 0.05	0.05 ± 0.02	3135.30	319,565.29	−4.00
Flare-V	3.18 ± 0.11	2.12 ± 0.05	0.09 ± 0.02	4095.35	342,522.71	−9.05
Flare-VI	2.81 ± 0.05	2.09 ± 0.02	0.08 ± 0.01	15,900.80	1,572,205.50	−30.90

5. Results and Discussion

We use 15 years of observations from the *Fermi*-LAT to explore the high-energy emission properties of B3 1343+451. We identify six major flares and calculate the decay and rising times of peaks. It is found that 15 peaks have rising and decay times of a few days, two peaks have sub-day rising and decay times, and one peak has rising and decay times above 10 days. The SEDs of all the flare phases are fitted with PL and LP models.

The brightest flare is observed during 23 July 2012–25 September 2012. The highest peak flux is $(8.29 \pm 0.49) \times 10^{-7}$ ph cm⁻² s⁻¹ with a symmetric temporal profile. The fastest rise and decay timescales are 0.20 ± 0.02 day (4.8 ± 0.48 h) and 0.22 ± 0.03 day (5.28 ± 0.72 h), respectively. Some similar studies reported light curves of 3C 273, 3C 454.3, PKS B1222+216, and S5 0836. The fastest flux-doubling timescale of the source can be used to constrain the size of the emission region. The size of the γ-ray-emitting region can be estimated by

$$R \leqslant ct_{\mathrm{var}}\delta/(1+z) \tag{8}$$

where z is the redshift of the source. The typical Doppler factors of $\delta \sim 10$–30, which are obtained by superluminal motion speeds, are observed in radio Very-Long-Baseline Interferometry (VLBI) monitoring observations [42,43]. The variability time t_{var} is the fastest halving/doubling timescale. Here, we adopt the redshift-corrected decay timescale 4.8 ± 0.48 h. The radius of the emission region R is estimated as $\sim5.18 \times 10^{15}$–1.56×10^{16} cm, which is less than the estimated value $R \sim 4.16 \times 10^{16}$ cm given by Sahakyan et al. (2020) with $\delta \sim 26$. Such small emission region sizes are rather difficult to accommodate in the standard framework, where the emission takes place at very large distances ($\sim$10–20 pc) from the central engine [30,44] unless the collimation angle of the jet is extremely small. For a blazar, the bulk Lorentz factor Γ generally approximates as $\Gamma \sim \delta$; thus, an upper limit on the viewing angle of the jet can be estimated as $\theta_{jet} \sim 1/\delta$. Considering the typical Doppler factors of $\delta \sim 10$–30, we obtain the viewing angle $\theta_{jet} \sim 1.9°$–$5.7°$.

The distance of the emission region can be constrained by using the observed variability timescale $d_\gamma \sim 2ct_{var}\Gamma^2/(1+z)$. Here, the bulk Lorentz factor $\Gamma \sim \delta$. Considering $\delta \sim 10$–30, we obtain $d_\gamma \sim 0.01$–0.09 pc. Considering a conical geometry, using the opening angle $\theta_{jet} \gtrsim R/d_\gamma$, we obtain an upper limit on the distance of the γ-ray emission region $d_\gamma \sim ct_{var}\delta/\theta_{jet}(1+z) \sim 0.00008$–$0.0007$ pc. It is worth pointing out that the R and θ_{jet} values found in this section could be smaller since the variability timescale t_{var} only gives a lower

limit. Our results suggest that the location of the γ-ray emission region may be close to the central black hole.

The DCF shows that the γ-ray emission regions of Flare-II and Flare-III with a time lag of 0 are located in the BLR. The DCFs from Flare-II and Flare-VI with a positive time lag and Flare-V with a negative time lag have a large amount of uncertainty, implying that we still cannot know whether the γ-ray region is located in the BLR or MT region. Here, we do not analyze the cross-correlation between optical, radio, and γ-ray. Some research has stated that observed radio/γ-ray correlations can be attributed to jet components that are being newly ejected from the central engine and a quadratic dependence of the amplitude of the γ-ray variability with respect to that of the optical, which favors an SSC explanation (see [45,46]). Although Wu et al. [29] found that the γ-ray spectrum is better reproduced when the dissipation region of the jet is located in the molecular torus, we find that the data of broadband SEDs from the seven flares are not simultaneous. In this case, the result of Wu et al. (2024) is controversial.

Figure 5 shows the histogram of all the 7-day binned flux data points and all the photon energy above 10 GeV and the peak fluxes, as also enumerated in Figure 1 and Table 1. In Figure 5a, we show that the flux distributions have a slowly rising part up to the peak and a fast-decaying part beyond the peak. Similar results were found for sources PKS 1510-089 and 3C 454.3, researched by Tavecchio et al. (2010) and Prince et al. (2017) [30,44]. Figure 5b shows the histogram of high-energy photons. Pezzuto et al. (2023) obtained that the best-fitting model is the power law for photon energy [47]. The peak fluxes are distributed around a mean of $4.99 \pm 1.60 \times 10^{-7}$ ph cm^{-2} s^{-1}, as shown in Figure 5c.

Figure 6a shows a histogram of the rise and decay times (see Table 1). We can clearly see that the distributions of the rise and decay times are not Gaussian. The rise and decay times are distributed with means of 4.17 ± 2.76 days and 4.97 ± 4.29 days, respectively. In Figure 6b, we show that a large number of peaks exhibit a symmetric temporal profile, which implies that the time of the jet plasma entering/leaving the standing shock is the same. The symmetric temporal profiles observed for the flares from source B3 1343+451 suggest that the rise and decay timescales are dominated by a disturbance from a dense plasma blob passing through the standing shock front in the jet region. However, in order to complete the blazar's flare process, the symmetric temporal profiles may be due to double action from a disturbance from a dense plasma blob passing through the standing shock front in the jet region and a jet moving within and out of the line of sight of observation. The asymmetric temporal profiles are expected to arise from the fast injection of accelerated particles, namely t_{acc} (acceleration timescales) $< t_{cool}$ (cooling timescale). We also plot the histogram redshift-corrected doubling/halving timescale τ_z (see Table 2) with means of 0.33 ± 0.05 and 0.33 ± 0.06 days in Figure 6c.

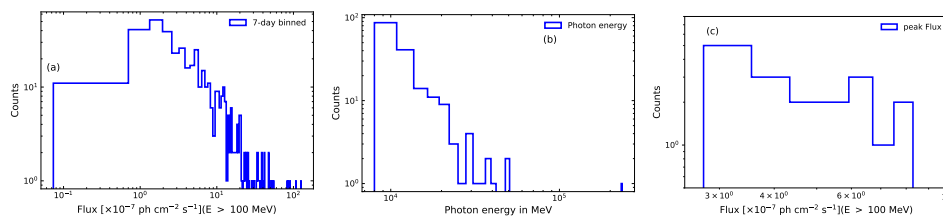**Figure 5.** (**a**) Histogram of all the 7-day binned flux data points. (**b**) Histogram of all the photon energy above 10 GeV. (**c**) Histogram of peak fluxes from Table 1.
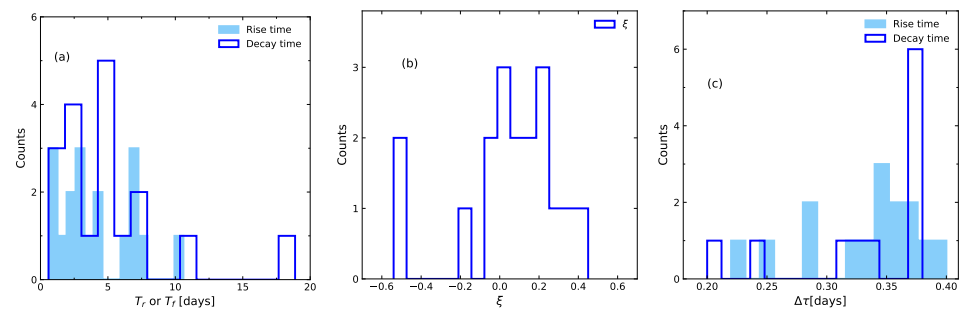
Figure 6. (**a**) Histogram of rise and decay times from Table 1. (**b**) Histogram of the symmetry factor (ξ) from Table 1. (**c**) Histogram of the rise and decay times from the fastest variability timescale from Table 2.

6. Summary

In this paper, we study the long-term light curve and spectral variations of B3 1343+451 using the data collected by the *Fermi*-LAT between 2008 and 2022. Six major flares with many substructures are detected in the weekly binning. The light curves with 2-day and 1-day binning are further studied to explore the triggering mechanism(s) and the physical properties of the emission regions. The shortest variability timescale of 0.20 ± 0.02 day is found, which can put a constraint on the size of the emission region of $R \sim 5.18 \times 10^{15}$–$1.56 \times 10^{16}$ cm. We also obtain that the γ-ray emission region is located at $d_\gamma \sim 0.00008$–0.09 pc. The results of the DCFs appear to show that Flare-II and Flare-III have no energy dependence on the cooling timescale. However, Flare-I, Flare-V, and Flare-VI do not have strong evidence of energy dependence on the cooling timescale. The SEDs are fitted with two different functional forms of a PL and LP. We find that the best-fit model is the LP form for Flare-II, Flare-III, Flare-V, and Flare-VI, with a curvature significance of $>3\sigma$, but the SEDs of Flare-I and Flare-IV can reasonably be described by the PL model. Our results indicate that the emission regions vary from one flare to another, which is consistent with earlier results. The γ-ray flaring activity may be triggered by the interaction of moving blobs of plasma and shock. Further combined multiband contemporaneous (optical, radio, and X-ray) observations are needed to identify the origin of the γ-ray flaring activity clearly and put a stronger constraint on the location of the emitting region.

Appendix A. Identifying the 1-Day and 2-Day Binned Light Curves

Here, we present the 2-day binned light curves of Flare-I, Flare-II, Flare-V, and Flare-VI and the 1-day binned light curves of Flare-III, which are described in Sections 3.1–3.5. Considering that statistical fluctuations tend to dominate at the short timescales, all peaks are identified by the BB algorithm with the false alarm rate parameter $p_0 = 0.05$ (95%).
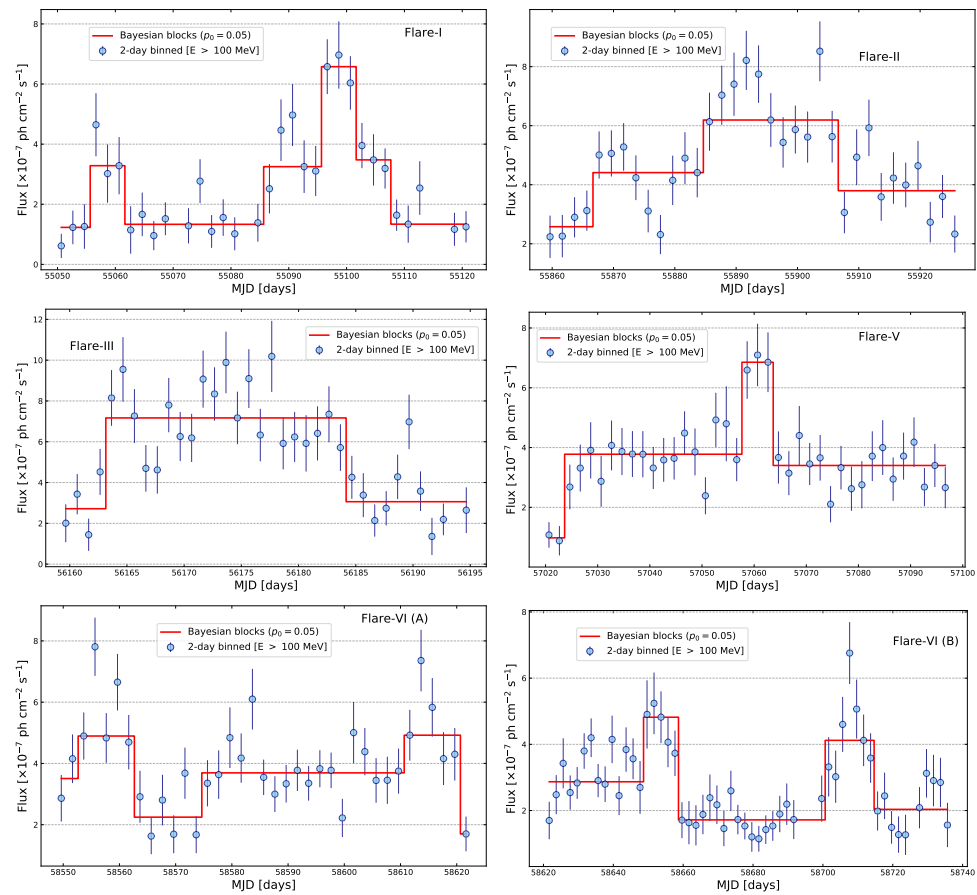
Figure A1. The 2-day binned light curves of Flare-I, Flare-II, Flare-V, and Flare-VI and the 1-day binned light curves of Flare-III. The peaks are identified by the BB algorithm with the false alarm rate parameter $p_0 = 0.05$.

Notes

1   https://fermi.gsfc.nasa.gov/cgi-bin/ssc/LAT/LATDataQuery.cgi (Accessed on 12 December 2022).
2   https://fermi.gsfc.nasa.gov/ssc/data/access/lat/BackgroundModels.html (Accessed on 20 December 2022).
3   https://fermi.gsfc.nasa.gov/ssc/data/analysis/scitools/source_models.html (Accessed on 20 December 2022).

References

1.   Matthews, J.H.; Bell, A.R.; Blundell, K.M. Particle acceleration in astrophysical jets. *New Astron. Rev.* **2020**, *89*, 101543. [CrossRef]
2.   Murase, K.; Stecker, F.W. High-Energy Neutrinos from Active Galactic Nuclei. In *The Encyclopedia of Cosmology. Set 2: Frontiers in Cosmology*; Stecker, F., Ed.; World Scientific: Singapore, 2023; pp. 483–540.
3.   Padovani, P.; Alexander, D.M.; Assef, R.J.; De Marco, B.; Giommi, P.; Hickox, R.C.; Richards, G.T.; Smolčić, V.; Hatziminaoglou, E.; Mainieri, V.; et al. Active galactic nuclei: What's in a name? *Astron. Astrophys. Rev.* **2017**, *25*, 2. [CrossRef]
4.   Ackermann, M.; Anantua, R.; Asano, K.; Baldini, L.; Barbiellini, G.; Bastieri, D.; Becerra Gonzalez, J.; Bellazzini, R.; Bissaldi, E.; Blandford, R.D.; et al. Minute-timescale >100 MeV γ-Ray Variability during the Giant Outburst of Quasar 3C 279 Observed by Fermi-LAT in 2015 June. *Astrophys. J. Lett.* **2016**, *824*, L20. [CrossRef]
5.   Shukla, A.; Mannheim, K.; Patel, S.R.; Roy, J.; Chitnis, V.R.; Dorner, D.; Rao, A.R.; Anupama, G.C.; Wendel, C. Short-timescale γ-Ray Variability in CTA 102. *Astrophys. J. Lett.* **2018**, *854*, L26. [CrossRef]
6.   Ding, N.; Gu, Q.S.; Geng, X.F.; Xiong, D.R.; Xue, R.; Wang, X.Y.; Guo, X.T. Exploring the Origin of Multiwavelength Activities of High-redshift Flat-spectrum Radio Quasar PKS 1502+106 during 2014–2018. *Astrophys. J.* **2019**, *881*, 125. [CrossRef]
7.   Geng, X.; Zeng, W.; Rani, B.; Britto, R.J.; Zhang, G.; Wen, T.; Hu, W.; Larsson, S.; Thompson, D.J.; Yang, S.; et al. Exploring High-energy Emission from the BL Lacertae Object S5 0716+714 with the Fermi Large Area Telescope. *Astrophys. J.* **2020**, *904*, 67. [CrossRef]
8.   Geng, X.; Ding, N.; Cao, G.; Liu, Y.; Bao, B.; Chidiac, C.; Kushwaha, P.; Shah, Z.; Zhang, Z.; Yang, X.; et al. Exploring γ-Ray Flares in the Long-term Light Curves of CTA 102 at GeV Energies. *Astrophys. J. Suppl. Ser.* **2022**, *260*, 48. [CrossRef]
9.   Pandey, A.; Stalin, C.S. Detection of minute-timescale γ-ray variability in BL Lacertae by Fermi-LAT. *Astron. Astrophys.* **2022**, *668*, A152.

10. Nalewajko, K.; Begelman, M.C.; Sikora, M. Constraining the Location of Gamma-Ray Flares in Luminous Blazars. *Astrophys. J.* **2014**, *789*, 161. [CrossRef]
11. Sahakyan, N.; Israyelyan, D.; Harutyunyan, G.; Khachatryan, M.; Gasparyan, S. Multiwavelength study of high-redshift blazars. *Mon. Not. R. Astron. Soc.* **2020**, *498*, 2594–2613. [CrossRef]
12. Finke, J.D.; Dermer, C.D.; Böttcher, M. Synchrotron Self-Compton Analysis of TeV X-Ray-Selected BL Lacertae Objects. *Astrophys. J.* **2008**, *686*, 181–194. [CrossRef]
13. Urry, C.M.; Padovani, P. Unified Schemes for Radio-Loud Active Galactic Nuclei. *Publ. Astron. Soc. Pac.* **1995**, *107*, 803. [CrossRef]
14. Ajello, M.; Baldini, L.; Ballet, J.; Bastieri, D.; Gonzalez, J.B.; Bellazzini, R.; Buson, S.; Caputo, R.; Caraveo, P.A.; Cheung, C.C.; et al. The Fourth Catalog of Active Galactic Nuclei Detected by the Fermi Large Area Telescope: Data Release 3. *Astrophys. J. Suppl. Ser.* **2022**, *263*, 24. [CrossRef]
15. Abdo, A.A.; Ackermann, M.; Ajello, M.; Atwood, W.B.; Axelsson, M.; Baldini, L.; Ballet, J.; Barbiellini, G.; Bastieri, D.; Bechtol, K.; et al. Spectral Properties of Bright Fermi-Detected Blazars in the Gamma-Ray Band. *Astrophys. J.* **2010**, *710*, 1271–1285. [CrossRef]
16. Ghisellini, G.; Madau, P. On the origin of the gamma-ray emission in blazars. *Mon. Not. R. Astron. Soc.* **1996**, *280*, 67–76. [CrossRef]
17. Ghisellini, G.; Ghirlanda, G.; Oganesyan, G.; Ascenzi, S.T.E.F.A.N.O.; Nava, L.; Celotti, A.; Salafia1, O.S.; Ravasio, M.E.; Ronchi, M. Proton-synchrotron as the radiation mechanism of the prompt emission of gamma-ray bursts? *Astron. Astrophys.* **2020**, *636*, A82. [CrossRef]
18. Sokolov, A.; Marscher, A.P. External Compton Radiation from Rapid Nonthermal Flares in Blazars. *Astrophys. J.* **2005**, *629*, 52–60. [CrossRef]
19. Dermer, C.D.; Cerruti, M.; Lott, B.; Boisson, C.; Zech, A. Equipartition Gamma-Ray Blazars and the Location of the Gamma-Ray Emission Site in 3C 279. *Astrophys. J.* **2014**, *782*, 82. [CrossRef]
20. Cao, G.; Wang, J.-C. On the location of the γ-ray emission region for 21 flat spectrum radio quasars with quasi-simultaneous observations. *Mon. Not. R. Astron. Soc.* **2013**, *436*, 2170–2178. [CrossRef]
21. Böttcher, M.; Reimer, A.; Sweeney, K.; Prakash, A. Leptonic and Hadronic Modeling of Fermi-detected Blazars. *Astrophys. J.* **2013**, *768*, 54. [CrossRef]
22. Cao, G.; Wang, J.-C. The Hadronic Origin of the Hard Gamma-Ray Spectrum from Blazar 1ES 1101-232. *Mon. Not. R. Astron. Soc.* **2014**, *783*, 108. [CrossRef]
23. Cerruti, M.; Zech, A.; Boisson, C.; Inoue, S. A hadronic origin for ultra-high-frequency-peaked BL Lac objects. *Mon. Not. R. Astron. Soc.* **2015**, *448*, 910–927. [CrossRef]
24. Paliya, V.S.; Zhang, H.; Böttcher, M.; Ajello, M.; Domínguez, A.; Joshi, M.; Hartmann, D.; Stalin, C.S. Leptonic and Hadronic Modeling of Fermi-LAT Hard Spectrum Quasars and Predictions for High-energy Polarization. *Astrophys. J.* **2018**, *863*, 98. [CrossRef]
25. Atwood, W.B.; Abdo, A.A.; Ackermann, M.; Althouse, W.; Anderson, B.; Axelsson, M.; Baldini, L.; Ballet, J.; Band, D.L.; Barbiellini, G.; et al. The Large Area Telescope on the Fermi Gamma-Ray Space Telescope Mission. *Astrophys. J.* **2009**, *697*, 1071–1102. [CrossRef]
26. Mattox, J.R.; Bertsch, D.L.; Chiang, J.; Dingus, B.L.; Digel, S.W.; Esposito, J.A.; Fierro, J.M.; Hartman, R.C.; Hunter, S.D.; Kanbach, G.; et al. The Likelihood Analysis of EGRET Data. *Astrophys. J.* **1996**, *461*, 396. [CrossRef]
27. Scargle, J.D.; Norris, J.P.; Jackson, B.; Chiang, J. Studies in Astronomical Time Series Analysis. VI. Bayesian Block Representations. *Astrophys. J.* **2013**, *764*, 167. [CrossRef]
28. Meyer, M.; Scargle, J.D.; Blandford, R.D. Characterizing the Gamma-Ray Variability of the Brightest Flat Spectrum Radio Quasars Observed with the Fermi LAT. *Astrophys. J.* **2019**, *877*, 39. [CrossRef]
29. Wu, F.; Hu, W.; Dai, B. The Nature of the High-energy γ-Ray Radiation Associated with the High-redshift Blazar B3 1343+451. *Astrophys. J.* **2024**, *972*, 183. [CrossRef]
30. Tavecchio, F.; Ghisellini, G.; Bonnoli, G.; Ghirlanda, G. Constraining the location of the emitting region in Fermi blazars through rapid γ-ray variability. *Mon. Not. R. Astron. Soc.* **2010**, *405*, L94–L98. [CrossRef]
31. Dotson, A.; Georganopoulos, M.; Kazanas, D.;Perlman, E.S. A Method for Localizing Energy Dissipation in Blazars Using Fermi Variability. *Astrophys. J.* **2012**, *758*, L15. [CrossRef]
32. Sun, M.; Xue, Y.; Cai, Z.; Guo, H. A Falling Corona Model for the Anomalous Behavior of the Broad Emission Lines in NGC 5548. *Astrophys. J.* **2018**, *857*, 86. [CrossRef]
33. Lee, J.W.; Lee, S.-S.; Hodgson, J.A. Interferometric Monitoring of Gamma-Ray Bright AGNs: S5 0716+714. *Astrophys. J.* **2017**, *841*, 119. [CrossRef]
34. Li, S.; Lee, S.-S.; Cheong, W.Y. A Multi-Wavelength Study on a Gamma-Ray Bright AGN 1308+326 Using KVN at 22 and 43 GHz. *J. Korean Astron. Soc.* **2024**, *57*, 67–82.
35. Brown, A.M. Locating the γ-ray emission region of the flat spectrum radio quasar PKS 1510-089. *Mon. Not. R. Astron. Soc.* **2013**, *431*, 824–835. [CrossRef]
36. Poutanen, J.; Stern, B. GeV Breaks in Blazars as a Result of Gamma-ray Absorption Within the Broad-line Region. *Astrophys. J. Lett.* **2010**, *717*, L118–L121. [CrossRef]
37. Senturk, G.D.; Errando, M.; Boettcher, M.; Coppi, P.; Mukherjee, R.; Roustazadeh, P. GeV-TeV Blazar Population Studies. *arXiv* **2011**, arXiv:1111.0378.

38. Harris, J.; Daniel, M.K.; Chadwick, P.M. Identifying Breaks and Curvature in the Fermi Spectra of Bright Flat Spectrum Radio Quasars. *Astrophys. J.* **2012**, *761*, 2. [CrossRef]
39. Sahakyan, N.; Harutyunyan, G.; Israelyan, D.; Khachatryan, M. Exploring the Origin of Multiwavelength Emission from High-Redshift Blazar B3 1343 + 451. *Astrophysics* **2020**, *63*, 334–348. [CrossRef]
40. Finke, J.D.; Dermer, C.D. On the Break in the Fermi-Large Area Telescope Spectrum of 3C 454.3. *Astrophys. J. Lett.* **2010**, *714*, L303–L307. [CrossRef]
41. Cerruti, M.; Dermer, C.D.; Lott, B.; Boisson, C.; Zech, A. Gamma-Ray Blazars near Equipartition and the Origin of the GeV Spectral Break in 3C 454.3. *Astrophys. J. Lett.* **2013**, *771*, L4. [CrossRef]
42. Böttcher, M. Progress in Multi-Wavelength and Multi-Messenger Observations of Blazars and Theoretical Challenges. *Galaxies* **2019**, *7*, 20. [CrossRef]
43. Cao, G.; Geng, X.; Wang, J.; Yang, X. Progress in multi-messenger observations and emission models of blazars. *New. Astron. Rev.* **2024**, *98*, 101693. [CrossRef]
44. Prince, R.; Majumdar, P.; Gupta, N. Long-term Study of the Light Curve of PKS 1510-089 in GeV Energies. *Astrophys. J.* **2017**, *844*, 62. [CrossRef]
45. Rani, B.; Krichbaum, T.P.; Fuhrmann, L.; Böttcher, M.; Lott, B.; Aller, H.D.; Aller, M.F.; Angelakis, E.; Bach, U.; Bastieri, D.; et al. Radio to gamma-ray variability study of blazar S5 0716+714. *Astron. Astrophys.* **2013**, *552*, A11.
46. Kim, D.W.; Kravchenko, E.V.; Kutkin, A.M.; Böttcher, M.; Gómez, J.L.; Gurwell, M.; Jorstad, S.G.; Lähteenmäki, A.; Marscher, A.P.; Ramakrishnan, V.; et al. Radio and γ-Ray Activity in the Jet of the Blazar S5 0716+714. *Astrophys. J.* **2022**, *925*, 64. [CrossRef]
47. Pezzuto, S.; Coletta, A.; Klessen, R.S.; Schisano, E.; Benedettini, M.; Elia, D.; Molinari, S.; Soler, J.D.; Traficante, A. A new tool to derive simultaneously exponent and extremes of power-law distributions. *Mon. Not. R. Astron. Soc.* **2023**, *525*, 4744–4760. [CrossRef]